The Astrophysical Journal, 847:16 (12pp), 2017 September 20 https://doi.org/10.3847/1538-4357/aa88b5

Non-local Thermodynamic Equilibrium Stellar Spectroscopy with 1D and ⟨3D⟩ Models. II. Chemical Properties of the Galactic Metal-poor Disk and the Halo

Maria Bergemann[1], Remo Collet[2,3], Ralph Schönrich[4], Rene Andrae[1], Mikhail Kovalev[1], Greg Ruchti[5], Camilla Juul Hansen[6,7], and Zazralt Magic[8,9]
[1] Max-Planck Institute for Astronomy, D-69117, Heidelberg, Germany; bergemann@mpia-hd.mpg.de
[2] Stellar Astrophysics Center, Ny Munkegade 120, Aarhus University, DK-8000 Aarhus, Denmark
[3] Research School of Astronomy and Astrophysics, Australian National University, Canberra ACT 2601, Australia
[4] Rudolf-Peierls center for Theoretical Physics, University of Oxford, 1 Keble Road, Oxford OX1 3NP, UK
[5] Lund Observatory, Box 43, SE-221 00 Lund, Sweden
[6] Dark Cosmology Centre, Niels Bohr Institute, University of Copenhagen, Juliane Maries Vej 30, DK-2100 Copenhagen, Denmark
[7] Technische Universität Darmstadt, Schlossgartenstr. 2, Darmstadt D-64289, Germany
[8] Niels Bohr Institute, University of Copenhagen, Juliane Maries Vej 30, DK-2100 Copenhagen, Denmark
[9] Center for Star and Planet Formation, Natural History Museum of Denmark, Øster Voldgade 5-7, DK-1350 Copenhagen, Denmark
Received 2016 October 30; revised 2017 July 11; accepted 2017 August 10; published 2017 September 15

Abstract

From exploratory studies and theoretical expectations it is known that simplifying approximations in spectroscopic analysis (local thermodynamic equilibrium (LTE), 1D) lead to systematic biases of stellar parameters and abundances. These biases depend strongly on surface gravity, temperature and, in particular, for LTE versus non-LTE (NLTE), on metallicity of the stars. Here we analyze the [Mg/Fe] and [Fe/H] plane of a sample of 326 stars, comparing LTE and NLTE results obtained using 1D hydrostatic models and averaged ⟨3D⟩ models. We show that compared to the ⟨3D⟩ NLTE benchmark, the other three methods display increasing biases toward lower metallicities, resulting in false trends of [Mg/Fe] against [Fe/H], which have profound implications for interpretations by chemical evolution models. In our best ⟨3D⟩ NLTE model, the halo and disk stars show a clearer behavior in the [Mg/Fe]–[Fe/H] plane, from the knee in abundance space down to the lowest metallicities. Our sample has a large fraction of thick disk stars and this population extends down to at least [Fe/H] ~ -1.6 dex, further than previously proven. The thick disk stars display a constant [Mg/Fe] ≈ 0.3 dex, with a small intrinsic dispersion in [Mg/Fe] that suggests that a fast SN Ia channel is not relevant for the disk formation. The halo stars reach higher [Mg/Fe] ratios and display a net trend of [Mg/Fe] at low metallicities, paired with a large dispersion in [Mg/Fe]. These indicate the diverse origin of halo stars from accreted low-mass systems to stochastic/inhomogeneous chemical evolution in the Galactic halo.

Key words: Galaxy: abundances – Galaxy: evolution – Galaxy: kinematics and dynamics – radiative transfer – stars: abundances – stars: late-type

Supporting material: machine-readable tables

1. Introduction

Chemical abundances in cool stars are perhaps the most important observational constraint to studies of chemical evolution of galaxies. In particular, in the Milky Way the abundance of the observed data, like that from the *Gaia*-ESO and APOGEE surveys, has led to major progress in our understanding of the formation of the Galaxy and its underlying stellar populations: the bulge, the disk, and the halo (e.g., McWilliam & Rich 1994; McWilliam et al. 2008; Nissen & Schuster 2010; Casagrande et al. 2011; Gonzalez et al. 2011; Bensby et al. 2014; Recio-Blanco et al. 2014; Kordopatis et al. 2015; Ness et al. 2016). The observed chemical abundances are also essential tracers of chemical evolution and star formation of other galaxies (e.g., Conroy et al. 2014; Greene et al. 2015; Onodera et al. 2015).

Among the most critical discriminants of stellar populations in the Galaxy is the α-enhancement, i.e., the relative abundance of α-group elements to iron. In this respect, magnesium plays a key role as the classical α-chain element, produced in hydrostatic burning in massive stars that end their lives as core-collapse supernovae. In contrast, Fe is produced in explosive burning in both supernova types (Woosley & Weaver 1995). Because of their intrinsic strength, the spectral lines of iron and magnesium are easy to measure in the spectra of late-type stars, even at low metallicity. These two elements have comparatively high cosmic abundance and, owing to their complex atomic structure, show many strong lines across the full stellar spectrum, from UV to IR. Thus the observed ratio of Mg to Fe in low-mass stars, which occur in all stellar populations, is traditionally taken to be a tracer of the star formation history in galaxies (Matteucci 2014 and references therein).

In Bergemann et al. (2012, hereafter Paper 1), we began to systematically explore the effects of departures from 1D LTE on stellar parameters. We focused on the non-local thermodynamic equilibrium (NLTE) spectral line formation of Fe lines using model atmospheres derived from the mean stratification of three-dimensional (3D) stellar surface convection simulations. The effect on the determination of $T_{\rm eff}$, $\log g$, and metallicity [Fe/H][10] was quantified. In the subsequent papers, Ruchti et al. (2013) and Hansen et al. (2013), we applied the new NLTE methods to larger samples of stars. The last paper in the series (Bergemann et al. 2017, hereafter Paper 2), presented

[10] Metallicity refers to the ratio of the stellar iron to hydrogen abundance relative to the Sun.

the analysis of mean 3D and NLTE effects on the Mg lines in cool star spectra.

In this work, we use the methods developed in Papers 1 and 2 to carry out a detailed abundance analysis of a large stellar sample using a grid of 1D hydrostatic and mean (temporally and spatially averaged) 3D hydrodynamical models (in the following, we will refer to these stratifications as ⟨3D⟩ model atmospheres) and NLTE radiation transfer. It has now been firmly established that Mg lines in spectra of late-type stars are affected by NLTE (Mashonkina 2013). Also, recent works have shown that the effects due to the differences between mean 3D and 1D atmospheric structures are not negligible (Osorio et al. 2015). However, it is still unknown whether the combined NLTE and mean 3D effects are large enough to impact the observed [Mg/Fe] distributions in Galactic populations and, consequently, conclusions drawn from the analysis of observed data sets.

The paper is structured as follows. Section 2 presents the observed stellar sample. In Section 3, we describe the details of the abundance calculations. We discuss the [Fe/H]−[Mg/Fe] results and compare different models in Section 4. Section 5 is devoted to the analysis of the results in the context of the chemical evolution of the Milky Way disk and halo.

2. Observations and Stellar Parameters

The observed stars were taken from Ruchti et al. (2011) and Hansen et al. (2013). The former sample consists of 319 main-sequence dwarf, subgiant, and red giant stars, with metallicities ranging between [Fe/H] ~ -3 up to ~ -0.4 dex (Figure 1). The stars were selected from the RAVE Survey (Steinmetz et al. 2006) to study a large sample of metal-poor stars with thick disk-like kinematics and observed at high-resolution ($R > 30{,}000$) at several facilities, including FEROS on the MPG 2.2 m telescope, the MIKE spectrograph on the *Magellan*-Clay telescope, the ARC spectrograph on the Apache Point 3.5 m telescope, and the UCLES spectrograph on the Anglo-Australian telescope. All spectra except those taken with UCLES cover the full optical range from ∼3500 to ∼9500 Å. The UCLES data cover only the range from 4460 to 7250 Å. The selection for this study was based on metallicities, $[M/H]_{cal} < -0.7$ (Zwitter et al. 2008), distances, and 3D space motions derived using the stellar parameters in the first and second data releases from RAVE.[11] All spectra yielded a signal-to-noise ratio S/N > 80 around ∼6000 Å.

We assumed two different sets of input stellar parameters: 1D LTE and NLTE-opt, as described in Ruchti et al. (2013). 1D LTE values were determined by the classical method of LTE excitation−ionization balance of Fe lines. Our second input data set was NLTE-opt, for which accurate estimates for the effective temperature ($T_{\rm eff}$), surface gravity ($\log g$), and metallicity of the stars were determined as follows. For $T_{\rm eff} > 4500$ K, the NLTE-opt temperature was estimated from the combination of fits to the wings of Balmer lines and the photometric $T_{\rm eff}$ calibration from Ruchti et al. (2011). Below 4500 K, the Ruchti et al. (2011) calibration was adopted. The surface gravity, metallicity, and micro-turbulence were estimated through the NLTE ionization balance of Fe I and Fe II lines. The adopted stellar parameters are listed in Table 1.

[11] Systematics in the RAVE stellar parameters (see Ruchti et al. 2011; Serenelli et al. 2013) resulted in the final sample containing a mixture of both disk and halo stars.

The second sub-sample[12] was selected from Hansen et al. (2012, 2013) and included seven dwarfs with a wide range of metallicities reaching [Fe/H] ~ -3 and -0.7 that belong to the halo and disk, respectively. Most of these stars have been observed with UVES/VLT in settings U-564, U-580, U-800, and U-860. This ensures a wavelength coverage that contains all the Mg lines under study while three of the stars have been observed using HIRES/Keck covering 3120–4650 Å. The slit width used is between 0.7 to 1.0 arcsec which ensures that all spectra are of high resolution ($R \sim 40{,}000$–$62{,}000$). Most spectra are of high S/N, with typical values of ∼200 at 5100 Å. For most of the stars the stellar parameters have been determined using photometry (IRFM) and parallax (see Hansen et al. 2012 for details). In a few cases (marked by "c" in Table B.1 in Hansen et al. 2012) we relied on stellar spectra to derive temperature and gravity owing to larger uncertainties in parallax and color. These stars had their parameters corrected and recomputed using NLTE corrections for Fe. Table 2 gives the adopted stellar parameters for the Hansen et al. (2013) sample.

We performed several tests in Ruchti et al. (2013), showing that the $T_{\rm eff}$ measurements were in agreement with the photometric, interferometric, and the infrared flux method temperatures. The accuracy of NLTE-opt surface gravities was tested by comparing them with astrometric (*Hipparcos*) and asteroseismic gravity estimates. For 214 stars in our sample, parallax estimates have become available from the Gaia Data Release 1 (Tycho−*Gaia* Astrometric Solution, TGAS) (Gaia Collaboration et al. 2016a, 2016b). Figure 2 compares our spectroscopic parallax estimates to the astrometric solution from TGAS, using either the 1D LTE or the NLTE-opt estimates. The NLTE-opt spectroscopic parallaxes are in good agreement with the TGAS data; stars with small parallaxes (luminous red giants beyond ∼2 kpc) deviate from the line due to their large uncertainties in the astrometric parallax.

Gaia parallaxes can be used to test the accuracy of the adopted surface gravity scale. Errors in the TGAS data set are very large for most stars in the sample, therefore we limit the comparison to those objects for which parallaxes are known to better than 30%. Figure 3 shows the comparison of the $\log g$ estimates based on the NLTE-opt method and the astrometric estimates derived using the TGAS parallaxes. The astrometric gravities are computed using the standard relationships:

$$M_{\rm V} = m_{\rm V} + 5\log(\pi) + 5 - A_{\rm V} \quad (1)$$

$$M_{\rm bol} = M_{\rm V} + {\rm BC} \quad (2)$$

$$\log L = -0.4(M_{\rm bol} - M_{\rm bol,\odot}) \quad (3)$$

$$[g] = [M] - [L] + 4[T_{\rm eff}] \quad (4)$$

where the square brackets represent the logarithmic ratio of a parameter with respect to the Sun, $m_{\rm V}$ is the apparent visual magnitude, M is the mass of a star taken from Serenelli et al. (2013), BC the bolometric correction, and L the luminosity. We adopt the photometry from Munari et al. (2014), and extinction in the V-band, $A_{\rm V}$, is computed using the coefficients in Schlafly & Finkbeiner (2011). Bolometric corrections are taken from Casagrande & VandenBerg (2014). The plot shows that there is a good agreement between the astrometric and spectroscopic NLTE-opt gravities. The few outliers appear to

[12] BD-133442, G 64-37, HD 3567, HD 19445, HD 106038, HD 121004, HD 122196.

Table 1
Stellar Parameters and Derived Mg Abundances for the Stellar Sample

Star	LTE-Fe				NLTE-opt				model (a)		model (b)		model (c)		model (d)	
	$T_{\rm eff}$	$\log g$	[Fe/H]	$\xi_{\rm t}$	$T_{\rm eff}$	$\log g$	[Fe/H]	$\xi_{\rm t}$	[Mg/Fe]	σ	[Mg/Fe]	σ	[Mg/Fe]	σ	[Mg/Fe]	σ
RAVE J002330.7-163143	5128	2.40	−2.63	1.30	5443	3.20	−2.29	0.90	0.35	0.15	0.25	0.12	0.29	0.12	0.37	0.11
RAVE J031535.8-094744	4628	1.51	−1.40	1.50	4774	2.06	−1.31	1.60	0.34	0.17	0.30	0.15	0.25	0.14	0.16	0.14
RAVE J040840.5-462532	4466	0.50	−2.25	2.20	4600	1.03	−2.10	2.10	NaN	NaN	NaN	NaN	NaN	NaN	NaN	NaN
RAVE J054957.6-334008	5151	2.53	−1.94	1.30	5393	3.16	−1.70	1.10	0.40	0.14	0.31	0.15	0.29	0.12	0.33	0.11
RAVE J114108.9-453528	4439	0.50	−2.42	2.10	4562	1.10	−2.28	1.90	NaN	NaN	NaN	NaN	NaN	NaN	NaN	NaN
RAVE J162051.2-091258	4551	0.67	−2.86	1.80	4951	2.04	−2.42	1.20	0.50	0.17	0.25	0.17	0.29	0.17	0.13	0.17
RAVE J194701.6-235336	4562	1.07	−1.96	1.80	4797	1.90	−1.75	1.80	NaN	NaN	0.31	0.15	0.26	0.13	0.28	0.14

Note. Columns 2–5 give stellar parameters determined using the 1D LTE excitation−ionization balance of iron. Columns 6–9 are the NLTE-opt stellar parameters (Ruchti et al. 2013).
(This table is available in its entirety in machine-readable form.)

Table 2
Results of Mg Abundance Determinations for the Stellar Sample from Hansen et al. (2013)

Star	$T_{\rm eff}$	log g	log $g_{\rm cor}$	$[{\rm Fe/H}]_{\rm LTE}$	$[{\rm Fe/H}]_{\rm NLTE}$	$\xi_{\rm t}$	[Mg/Fe]			
							model (a)	model (b)	model (c)	model (d)
BD−133442	6450	4.20*	4.42	−2.56	−2.46	1.5	0.33	0.24	0.30	0.46
G 64−37	6494	3.82*	4.23	−3.17	−3.00	1.4	0.63	0.32	0.41	0.57
HD 3567	6035	4.08	4.08	−1.33	−1.29	1.5	0.26	0.22	0.20	0.20
HD 19445	5982	4.38	4.38	−2.13	−2.10	1.4	0.46	0.43	0.45	0.45
HD 106038	5950	4.33	4.33	−1.48	−1.45	1.1	0.49	0.45	0.43	0.44
HD 121004	5711	4.46	4.46	−0.73	−0.71	0.7	0.25	0.24	0.23	0.27
HD 122196	6048	3.89	3.89	−1.81	−1.75	1.2	0.28	0.23	0.25	0.27

Note. The log g and $[{\rm Fe/H}]_{\rm LTE}$ in columns 3 and 5 were computed in LTE. Columns 4 and 6 give NLTE estimates of gravity and metallicity.

be binaries or stars in multiple systems, according to the large astrometric excess noise in the *Gaia* DR1.

Metallicities, even though based on 1D NLTE analysis, are expected to be sufficiently accurate for our purposes, and we do not recompute them. In Bergemann et al. (2012c), we showed that the difference between the 1D NLTE and ⟨3D⟩ NLTE metallicities is very small, and is of the order 0.01–0.04 dex for the full range of stellar parameters analyzed here. In this work, metallicities are used to compute the model atmospheres for Mg abundance determinations and then to calculate the [Mg/Fe] abundance ratios.

3. Methods

3.1. Model Atmospheres and Linelist

We use two different sets of model atmospheres. The reference 1D models are hydrostatic plane-parallel MAFAGS-OS model atmospheres (Grupp 2004a, 2004b). Mean 3D models were derived by averaging the physical structure from 3D Stagger stellar surface convection simulations (Collet et al. 2011; Magic et al. 2013). A description of the averaging procedure of time-dependent 3D model atmospheres is given in Bergemann et al. (2012a). The applicability of mean 3D models in spectroscopic analysis was studied in Paper 2 using the full 3D NLTE radiative transfer for selected Mg spectral lines.

With the goal of establishing reliable abundances, we have taken special care to select only the most robust Mg I spectral lines. These are the lines that are not excessively affected by blending, are not located in regions with poorly defined quasi-continuum, and are visible at low metallicity. Also in Paper 2, we showed that the 5711 Å and, to a lesser degree, the 5528 Å features should be preferred for abundance analyses in cool-type stars, because other features (including the resonance line at 4571 Å and the optical triplet at 5172 and 5183 Å) are more sensitive to the structure of stellar atmospheres, and thus to the limitations caused by the use of the hydrostatic models. Therefore in this paper, we limit the analysis to the spectral lines at 5711 and 5528 Å. The atomic data are those given in Paper 2: log gf (5711 Å) = −1.742, and log gf (5528 Å) = −0.547; both estimates of transition probabilities are adopted from Pehlivan Rhodin et al. (2017). The damping caused by inelastic collisions with hydrogen atoms is from Barklem et al. (2000) for the 5528 Å line; for the 5711 Å line, we use the damping constants kindly provided by P. Barklem (2017, private communication).

The NLTE statistical equilibrium is computed using the DETAIL code (Butler & Giddings 1985) and the updated Mg atomic model by Bergemann et al. (2015) which builds upon the model by Mashonkina (2013). Line profile fitting and abundance determinations are performed using the spectrum synthesis code SME (Valenti & Piskunov 2012). When fitting each Mg I line, we allow for individual variations of macro-turbulence. However, the $V_{\rm mac}$ estimates for both Mg I lines are not very different and show only a small systematic offset of $\sim$1 km s^{-1} that is likely caused by the differences in the velocity field at the depth of line formation. We ensure the quality of all line fits by visual inspection. We also determine the line equivalent widths (EWs) through the integration of the observed line profiles and of the best-fit models. This procedure is very useful to eliminate poor fits caused, for example, by line veiling or contamination by blends. Furthermore, all measurements for which the EW is less than 5 mÅ or the difference between the observed and synthetic EW is larger than 3% are disregarded. The EW measurements are given in Table 3.

3.2. Abundance Determination

The Mg abundances are computed using two different sets of stellar parameters, 1D LTE and NLTE-opt (Section 2).

To derive 1D and ⟨3D⟩ NLTE Mg abundances, we first compute the LTE Mg abundance for each Mg I line using our best NLTE-opt stellar parameters. Some examples of the best-fit line profile fits are shown in Figure 4. Then we compute the 1D NLTE and ⟨3D⟩ NLTE Mg abundance corrections separately, and apply the corrections to the LTE Mg abundances. The abundance correction is defined as the difference between the abundance of a spectral line obtained using the NLTE calculations (with either 1D hydrostatic or ⟨3D⟩ model atmospheres) and that obtained in 1D LTE (both sets computed with the more accurate NLTE-opt stellar parameters), and is hereafter denoted by:

$$\Delta A({\rm Mg}) = A({\rm Mg})_{\rm NLTE} - A({\rm Mg})_{\rm LTE}. \quad (5)$$

Since the corrections are also sensitive to the atmospheric abundance of the element, we compute the correction relative to the Mg abundance found in our LTE calculations, not relative to the scaled-solar abundance of the element.

In 1D, the NLTE corrections typically range from −0.1 to 0.1 dex. Only for the model atmospheres with the lowest surface gravity (log g < 1 dex) and effective temperature ($T_{\rm eff}$ < 4500 K) do the 5711 and 5528 Å lines show a correction of −0.15 dex. The ⟨3D⟩ NLTE corrections are larger, ranging from −0.2 (cool low-gravity models) to 0.2 (metal-poor models of turnoff stars with $T_{\rm eff}$ > 6500 K) dex. Figures 7 and 8 (in the Appendix) illustrate this behavior for

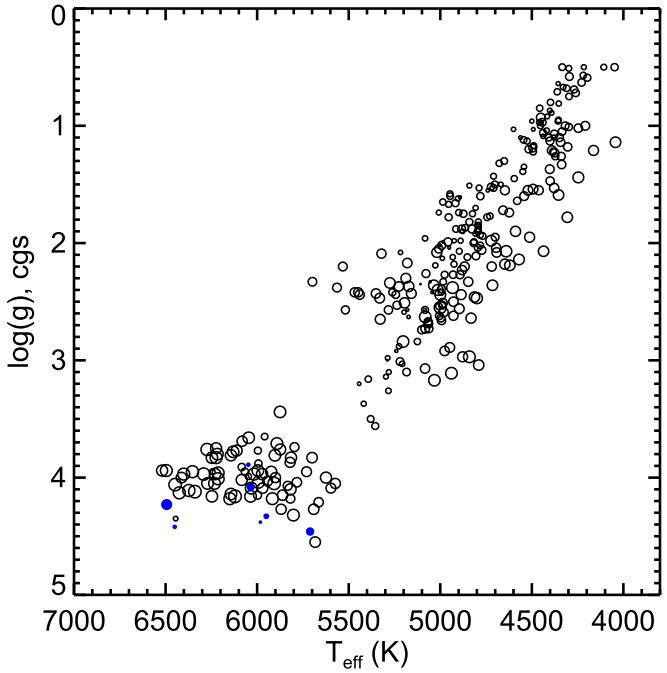

Figure 1. Location of the observed sample in the $T_{\rm eff}$–log g plane. NLTE stellar parameters from Ruchti et al. (2013) are shown as open circles and the stars from Hansen et al. (2013) as filled symbols. Symbol size is proportional to the metallicity [Fe/H], which spans the range from −3 to −0.5 dex.

the both types of models as a function of $T_{\rm eff}$, log(g), and [Fe/H].

The final Mg abundance is computed as the average of the measurements based on the 5711 and 5528 Å features. The uncertainties of the Mg measurements are derived as follows. The systematic errors are computed by propagating the uncertainties in $T_{\rm eff}$, log g, [Fe/H], and atomic data (transition probabilities) in the Mg abundance error, also including the 0.2 km s^{-1} error in micro-turbulence. The systematic error was computed by summing the error components in quadrature:

$$\sigma_{\rm tot} = (\sigma^2_{\xi_{\rm t}} + \sigma^2_{\rm [Fe/H]} + \sigma^2_{\log gf} + \sigma^2_{\log\ g} + \sigma^2_{T_{\rm eff}})^{1/2}. \quad (6)$$

In this approach, the uncertainties in stellar parameters are assumed to be uncorrelated, which may not be true, as shown by Schönrich & Bergemann (2014). However, the full probability distribution in parameter space is not available to us. A full treatment is beyond the scope of this paper, and in this case not necessary for our general conclusions. The internal error is given by the standard deviation of the measurement based on the 5711 and 5528 Å lines. If only one Mg I line is available (Table 3), the internal uncertainty is taken to be 0.05 dex. Then the total error is computed as the sum of the statistical and systematic error components.

4. Results

The derived Mg abundances are given in Tables 1 and 2 and are shown in Figure 5 as a function of metallicity. The error bar in the top right corner reflects the internal uncertainty (line-to-line dispersion) of the measurements. For giants with $T_{\rm eff} < 4500$ K or surface gravity <1.5, we cannot provide a robust estimate of the systematic uncertainty, because the

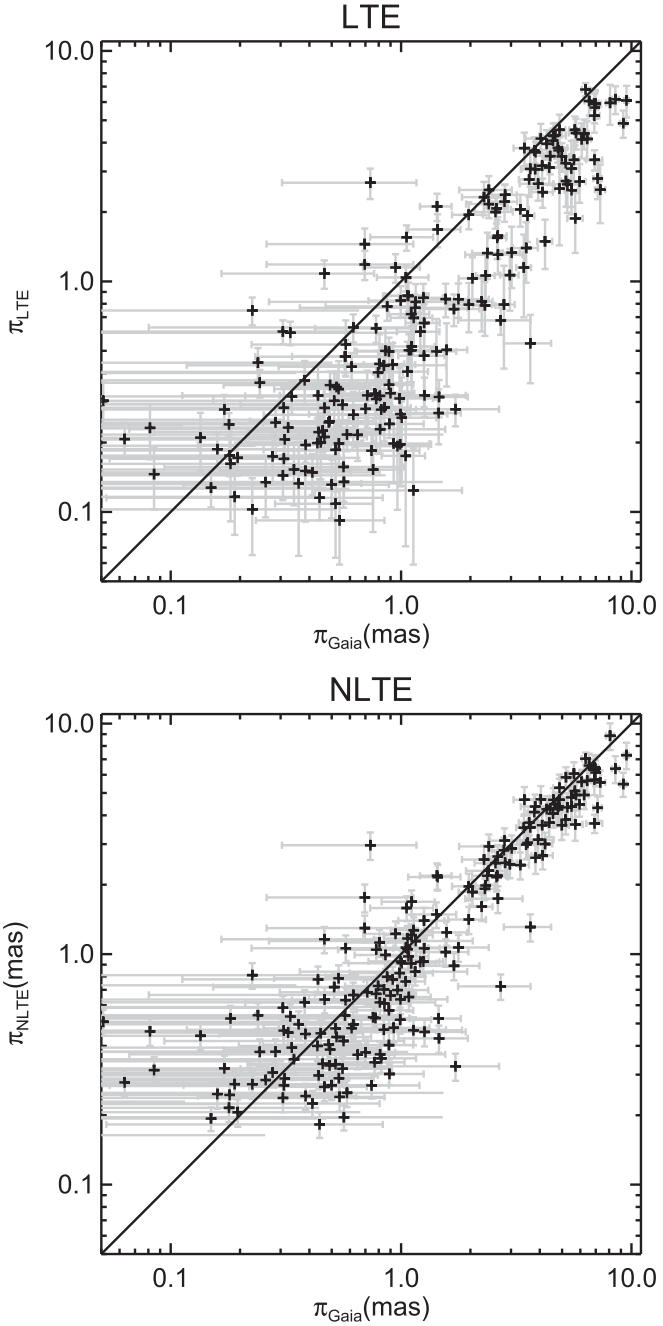

Figure 2. Comparison of spectroscopic parallax ($\pi_{\rm LTE}$, $\pi_{\rm NLTE}$) estimates for our stellar sample from Ruchti et al. (2013) with the *Gaia* TGAS solutions (Gaia Collaboration et al. 2016a, 2016b). Top panel: LTE stellar parameters; bottom panel: NLTE stellar parameters. The solid line represents the one-to-one relationship.

original ⟨3D⟩ model atmosphere grid does not sample this regime of stellar parameter space. Also for some very cool and low-gravity models we could not achieve convergence of NLTE level populations in the ⟨3D⟩ grid. These stars are therefore not shown in Figure 5.

The LTE [Mg/Fe]–[Fe/H] distributions computed using 1D LTE stellar parameters are shown in Figure 5(a). The other three panels (b)–(d) show Mg abundances computed using the more accurate NLTE-opt stellar parameters (see Section 2), with the 1D LTE, 1D NLTE, and ⟨3D⟩ NLTE approach for Mg abundance determinations. To make the average trend visible,

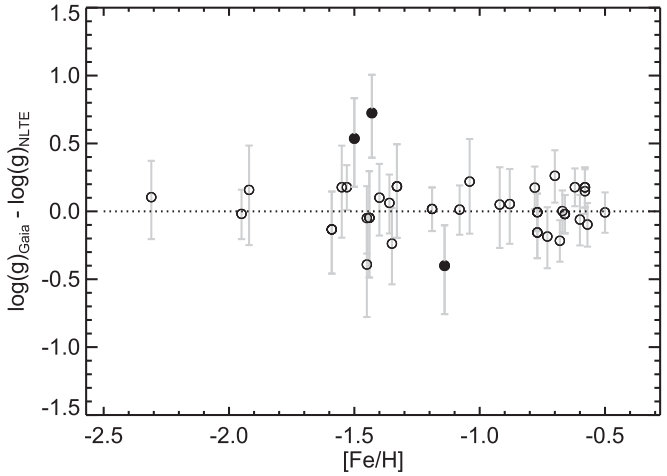

Figure 3. Difference between the astrometric estimate of surface gravity and the spectroscopic NLTE estimate for the stars with parallax errors within 30% and extinction less than 0.1. Candidate binaries or multiple systems are shown as filled circles. The error bars represent the combined uncertainties of the astrometric and spectroscopic $\log g$ estimates; typically, they are dominated by the errors of the TGAS parallaxes.

Figure 5 also shows the smoothed [Mg/Fe] distributions computed using the robust form of the LOESS regression (Cappellari et al. 2013). The smoothing parameter is set to 0.4. We ignore ten data points at the low- and high-metallicity end, in order to minimize the error caused by the data sparseness close to the edges of the distribution. The errors bars on the LOESS curve represent the sample estimated uncertainty of the mean computed in 0.3 dex metallicity intervals.

Comparison of the models (a) and (b) in Figure 5 clearly illustrates the important effect of stellar parameters ($T_{\rm eff}$, $\log g$, [Fe/H]) on the distribution of stars in the [Fe/H]–[Mg/Fe] plane. Assuming 1D LTE in stellar parameter and abundance determinations (Figure 5(a)), we find that the shape of the [Mg/Fe] distribution with metallicity has two components. In the metal-poor stars, [Mg/Fe] ratio mildy increases with decreasing metallicity. At metallicites higher than [Fe/H] ≈ -0.8 dex, the [Mg/Fe] ratio drops toward the solar value. The change of the slope occurs at slightly lower metallicity compared to what is known in the literature (Nissen et al. 1994; Fuhrmann 1998, 2004; Bensby et al. 2014; Kordopatis et al. 2015), but this is simply because of the metallicity selection in our sample, which creates a strong bias against metal-rich stars with [Fe/H] $\gtrapprox -0.7$. In other samples, which are more complete in the metallicity regimes probing the thin disk (e.g., Bensby et al. 2014), the [Mg/Fe] distribution changes slope at [Fe/H] ~ -0.6.

If we adopt more accurate NLTE-opt stellar parameters, but assume LTE line formation for Mg (Figure 5(b)), the location of the knee in the [Fe/H]–[Mg/Fe] does not change, but the slope of the metal-poor part of the [Mg/Fe] distribution does. For the most metal-poor stars ($-3 \leqslant$ [Fe/H] $\leqslant -1.5$), [Mg/Fe] is an increasing function of metallicity. This effect is a consequence of the NLTE effect on iron abundances (see Ruchti et al. 2013 for more details) which implies that the overall distribution becomes more metal-rich. The [Mg/Fe] estimates come out lower, most notably in the metal-poor regime, where the NLTE effects on iron abundance are significant.

The NLTE Mg abundances derived using the NLTE-opt stellar parameters (Figure 5(c)) are not very different from the model (b), with [Mg/Fe] only slightly deviating from the plateau at 0.3 dex below [Fe/H] ~ -1. The scatter of [Mg/Fe] is relatively constant with metallicity, of the order $\sim$0.15 dex, slightly larger than the internal uncertainty of the abundance measurements; however, the number of stars deviating from the trend line increases with decreasing [Fe/H]. Some of these stars have very low [Mg/Fe], close to the solar value, and a few very metal-poor objects have [Mg/Fe] ratios higher than the mean trend by $\gtrsim$0.2 dex.

The $\langle$3D$\rangle$ NLTE (Figure 5(d)) [Mg/Fe] distribution is quite different from the distribution obtained using model (c). First, the [Mg/Fe] ratio does not reach the 0.4 dex enhancement at the location of the break at [Fe/H] ~ -1, but remains at the level of 0.25 dex. Beyond this point, the [Mg/Fe] ratio appears to grow monotonically toward lower metallicities. There is an indication for the [Mg/Fe] ratio stalling or even falling beyond [Fe/H] ~ -1.8; however, the increasing scatter and dwindling stellar numbers reveal this change as barely significant, as indicated by the black error bars. We will see in the next section that this trend harbours the metal-poor thick disk tail with actually constant [Mg/Fe], overlaid by the halo population exhibiting a strong trend. At even lower metallicity, the star-to-star scatter increases and, again, we find a number of stars which are more enriched/or depleted in [Mg/Fe] ratios than the trend line. Whereas our $\langle$3D$\rangle$ NLTE [Mg/Fe] distribution contrasts with our 1D LTE/NLTE results and with other optical studies of Mg abundances in the disk stars, it is consistent with the results of the APOGEE survey (Holtzman et al. 2015; García Pérez et al. 2016) based on the infrared H-band stellar spectra. They also find maximum enrichment of [Mg/Fe] $\sim$ 0.25 dex at the metallicities of the thin and thick disk, although the analysis is based on 1D LTE.

Table 3
Measurements of the Equivalent Widths of the Two Mg I Diagnostic Lines for the Program Stars

	EW	
Star	Mg I 5528	Mg I 5711
RAVE J002330.7-163143	54.96	5.45
RAVE J031535.8-094744	159.80	71.13
RAVE J040840.5-462532	117.82	29.01
RAVE J054957.6-334008	99.60	23.14
RAVE J114108.9-453528	90.74	14.48
RAVE J162051.2-091258	60.12	2.34
RAVE J194701.6-235336	128.36	41.42

Note. The EWs are given in mÅ.

(This table is available in its entirety in machine-readable form.)

5. Interpretation and Implications for Chemical Evolution

The differences between the approaches to spectroscopic Mg abundance determinations have implications for Galactic chemical evolution. As an α-capture element (proton and neutron numbers are a multiple of helium), Mg I is thought to originate from essentially the same production sites as the other α-elements, i.e., mostly ejected from massive stars in their core collapse, while Fe is produced in both SNe Ia and in SNe II. The time delay of SNe Ia sets a natural clock (Tinsley 1979; Greggio & Renzini 1983) that makes the plane of [Mg/Fe] versus Fe a traditionally used diagnostic for the star formation history in the Galaxy. High Mg/Fe ratios mark earlier star

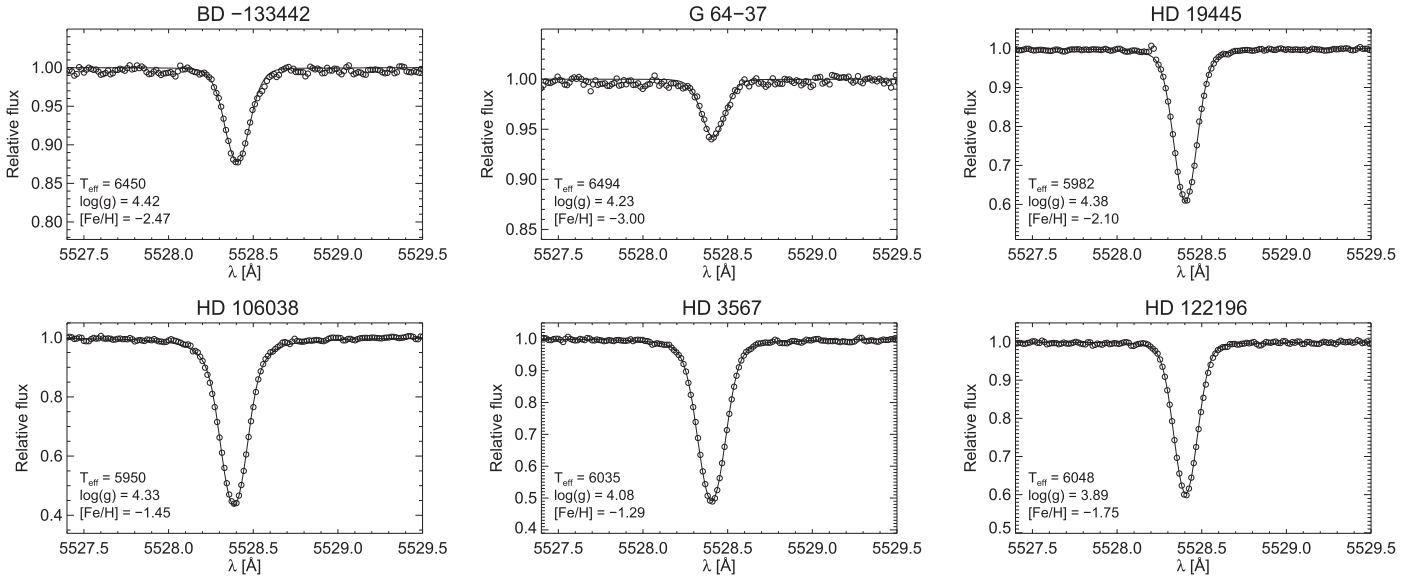

Figure 4. Observed profiles (open circles) and best-fit LTE profiles (solid line) for the 5528 Å Mg I line for the stars from the Hansen et al. (2013) sample.

formation in the halo and thick disk, before [Mg/Fe] begins to fall. Since metallicity enrichment runs on similar timescales, populations form the typical knee shape in the [Mg/Fe] versus Fe distribution. The downturn position of [Mg/Fe] is linked to the star formation intensity and yield loss rates of star-forming systems. The intense star formation and relatively low mass-loss rates in thick-disk-like (or central disk in the interpretation of Schönrich & Binney 2009a) regimes enable the system to reach high metallicity (~ -0.6 dex) before SN Ia enrichment sets in. In contrast, the high mass loss/low star formation intensity of dwarf galaxies, which contribute to the halo, sets this knee generally to [Fe/H] < -1 dex and gives them low α/Fe stars at low metallicities (Venn et al. 2004; Grebel 2005; Tolstoy et al. 2009; Matteucci 2014 and references therein).

An interesting question in chemical evolution is whether the high-α plateau is really a plateau or shows trends with metallicity. A deviation could be related, for example, to a very fast channel for SN Ia production (Matteucci et al. 2006) or to a metallicity dependence of SN II yields. A bimodal distribution of SN Ia delay times, with a significant early contribution from systems with lifetimes of only 10^8 Gyr, was proposed to explain the dependence of SN Ia rates on galaxy colors (Mannucci et al. 2005, 2006), and in the context of the Galactic chemical evolution this scenario implies that α/Fe ratio begins to decline already at very low metallicity [Fe/H] ~ -2. As for SNe II, the ratio of Mg I and Fe production is very sensitive to the specific SN II piston model (Woosley & Weaver 1995) and, since Mg stems from shells above the Ni/Fe core, critically depends on the cut-off for fall-back of material onto the neutron star/black hole (see Limongi & Chieffi 2003, for a discussion of the pre-collapse shell structure). Increasing escape of material from the core region of the massive stars (which is linked to the ^{56}Ni brightness) can hence lower the Mg/Fe ratios.

Our NLTE (Figure 5, panels (c), (d)) results imply different behavior of α/Fe below [Fe/H] ~ -1. On the surface, our NLTE determinations show a lower mean [Mg/Fe] at low metallicities. For the stars with $-2.5 <$ [Fe/H] < -2, we get the mean ratio [Mg/Fe] ~ 0.45 dex in 1D LTE, but only [Mg/Fe] ~ 0.30 in 1D NLTE or $\langle$3D$\rangle$ NLTE. This happens also in some classical evolution models; e.g., Timmes et al. (1995) indicate a depression to a solar value at [Fe/H] < -2 in all α-chain elements. This depression is more prominent if different fall-back schemes and low-energy SNe II are taken into account. Brusadin et al. (2013) show that a two-infall CGE model with the gas outflow during the halo formation phase predicts a depression at [Fe/H] from -1.8 to -1.0 with a "knot-like" structure that indicates the phase in the evolution of the Galactic halo where star formation was inactive. We do not find evidence for a substructure of this kind in our $\langle$3D$\rangle$ NLTE distributions of [Mg/Fe]. On the other hand, a depleted region in intermediate [Mg/Fe] is a natural feature of analytical chemical evolution models (Schönrich & Binney 2009a, 2009b), even more so in radial migration models on the low-metallicity side, where the locally observed high-α/Fe ridge is enhanced by outward migrators from the more populated inner disk.

However, this is not only a change of mean value, but a change of the variation of relative Mg abundances in single stars. The star-to-star scatter in [Mg/Fe] in the metallicity range [Fe/H] from -2.5 to -2 dex is 0.10 dex in $\langle$3D$\rangle$ NLTE. However, at [Fe/H] ~ -1.5 dex, the $\langle$3D$\rangle$ NLTE scatter of [Mg/Fe] drops to 0.05 dex, which is smaller than the internal uncertainties of the measurements, i.e., the measurements are consistent with no cosmic scatter. Also, as already noted, at [Fe/H] $\lesssim -1.8$, the dispersion of [Mg/Fe] abundance ratios grows. This suggests two options: (i) the presence of accreted stars (Nissen & Schuster 2010) from low-metallicity dwarf galaxies with extended star formation histories. These are shown to contain numerous low-α stars at low metallicity (Shetrone et al. 2003; de Boer et al. 2014; Lemasle et al. 2014). (ii) Intrinsic scatter, i.e., stochastic chemical evolution, ranging from scatter in local star formation intensities of Galactic protohalos (Gilmore & Wyse 1998) to more sophisticated stochastic chemical evolution models (Argast et al. 2000, 2002; Karlsson 2005; Karlsson & Gustafsson 2005; Cescutti 2008). Cosmological simulations of the Galaxy formation also predict significant dispersion of α-abundance ratios at low metallicity. These results depend on the prescriptions for metal diffusion and metallicity floor, but also with simple prescriptions, α-poor

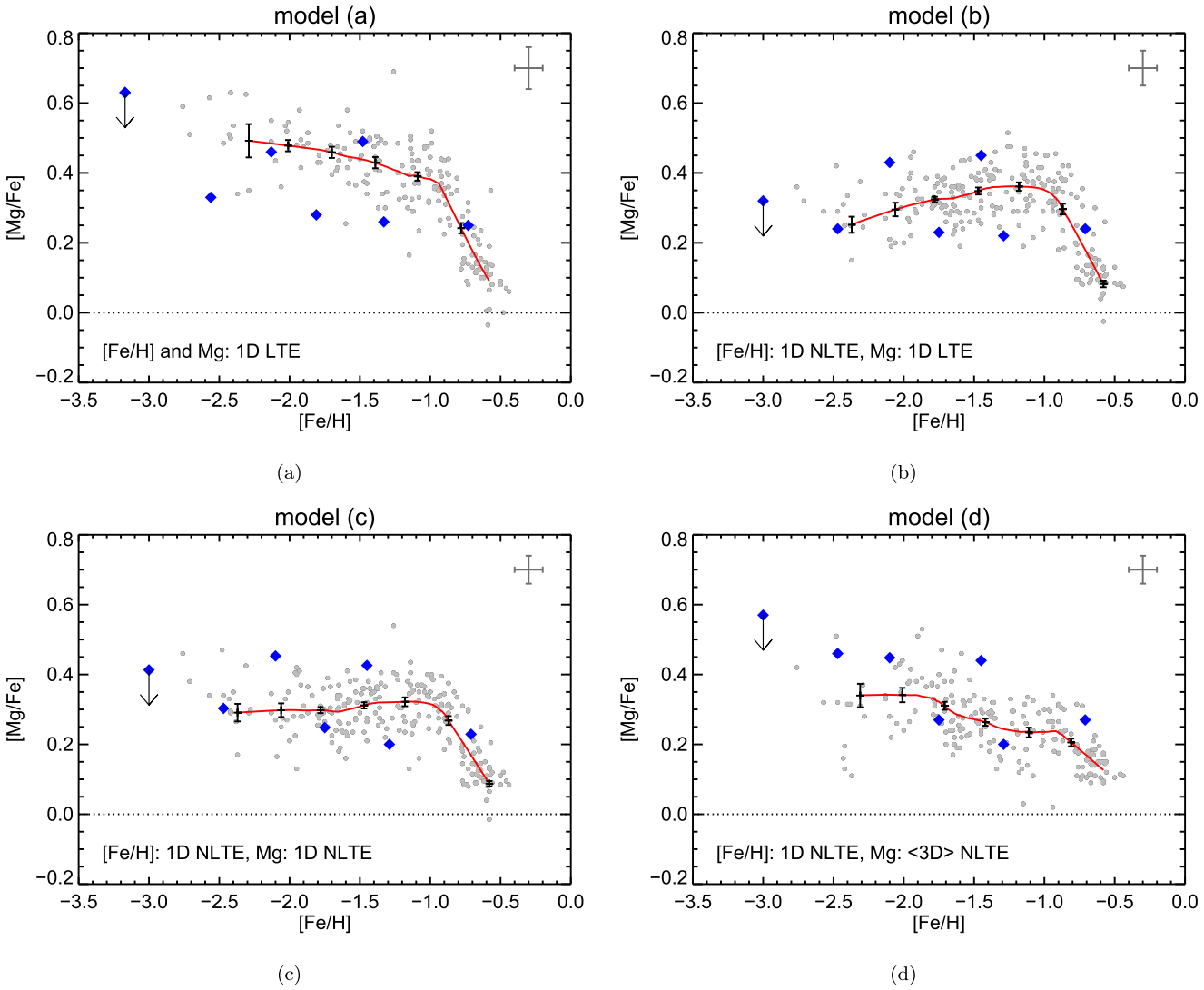

Figure 5. [Mg/Fe] abundance ratios as a function of metallicity determined using the four modeling scenarios: model (a) LTE stellar parameters and LTE Mg; model (b) NLTE-opt stellar parameters and LTE Mg; model (c) NLTE-opt stellar parameters and NLTE Mg; model (d) NLTE-opt stellar parameters and $\langle 3D \rangle$ NLTE Mg. The number of measurements shown in panel (d) differs from the other panels, because we could not achieve convergence of NLTE level populations in the $\langle 3D \rangle$ grid for some very cool and low-gravity models. The reference main-sequence stars from Hansen et al. (2013) are shown as filled blue diamonds. The error bar in the top right corner is the internal uncertainty of the measurements. The red line depicts the smoothed [Mg/Fe] distribution computed using LOESS regression. The errors bars attached to the LOESS curve represent the sample estimated uncertainty of the mean, i.e., the sample dispersion divided by $\sqrt{N-1}$, with N the number of stars in the metallicity bin of 0.3 dex.

and α-rich stars have a non-negligible probability to occur at [Fe/H] ~ -2 and lower (Shen et al. 2015).

Finally, in Figure 6 we show the $\langle 3D \rangle$ NLTE-derived abundance plane when separated into likely halo versus thin and thick disk stars via the kinematic classification of Ruchti et al. (2011). To minimize the impact of the systematic uncertainties, we have only plotted those stars where the 5711 Å line is available; this line, as shown in Paper 2, is least sensitive to the effects of convective inhomogeneities and the difference between $\langle 3D \rangle$ NLTE and full 3D NLTE is within $\sim$0.05 dex. Thus, the systematic errors are expected to be small. The plot also shows a LOESS curve computed as described in the previous section, but with a larger smoothing parameter, $\alpha = 0.8$, and ignoring five points at the edges, to mitigate the effect of smaller number statistics. This plot sheds some light on the previously discussed trend of [Mg/Fe] versus [Fe/H] at low metallicities: the thick disk ridge does not even show a hint of a slope in [Mg/Fe] down to its lowest metallicity members [Fe/H] ≈ -1.6 dex. This makes it difficult to uphold the argument for a fast SN Ia channel from low-metallicity disk star abundances (Matteucci et al. 2006). Instead, the trend we saw before in Figure 5(d) is created by the halo populations crossing from on average very high [Mg/Fe] and reaching down to near-solar abundances around [Fe/H] ≈ -1.0, a behavior that is observed and described for dwarf galaxies, e.g., in Venn et al. (2004), and which is due to their high mass loss rates and very low star formation efficiencies. The increased scatter in the halo [Mg/Fe] is consistent with an origin in a diverse population of small accreted galaxies and/or stochastic chemical evolution.

6. Conclusions

To shed light on how our understanding of Galactic chemical evolution is impacted by systematics in our assumptions of spectroscopic analysis, we have performed a comparative

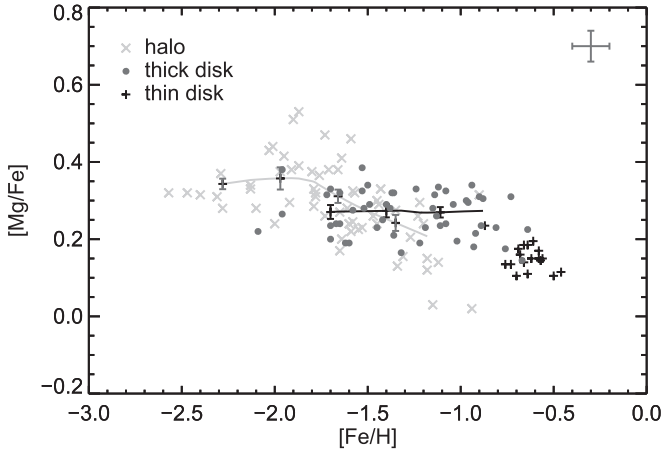

Figure 6. ⟨3D⟩ NLTE [Mg/Fe] abundance ratios as a function of metallicity, separated via a kinematic classification from Ruchti et al. (2011). We depict likely halo stars as gray crosses, likely thick disk stars as filled circles, and likely thin disk stars as plus signs. The errors bars represent the sample estimated uncertainty of the mean. The solid lines depicts the smoothed [Mg/Fe] distribution computed using LOESS regression.

analysis of [Fe/H] versus [Mg/Fe] for a large sample of 326 halo and thick disk stars using four different methods: LTE and NLTE with 1D hydrostatic model atmospheres, as well as with the averages of 3D hydrodynamical model stellar atmospheres. In the ⟨3D⟩ approach, we take into account the effects of hydrodynamic cooling associated with convective overshooting in the 3D simulations, but the effect of horizontal inhomogeneities is not addressed. However, recent studies (for Mg, see also Bergemann et al. 2017) suggest that the horizontal fluctuations only have a minor effect on the abundances of elements.

We find that these four modeling scenarios each lead to substantially and qualitatively different trends and distributions of [Mg/Fe] with [Fe/H]. Compared to the ⟨3D⟩ NLTE results, all other methods lead to significant biases in the [Mg/Fe]—[Fe/H] plane. The 1D LTE analysis overestimates the [Mg/Fe] abundance ratios at lower metallicities, implying a false, mildy increasing trend with declining [Fe/H], while the opposite bias happens in 1D NLTE. The differences between 1D NLTE and ⟨3D⟩ NLTE are also significant at low metallicity, [Fe/H] < -1.5. This is due to larger differences between the hydrostatic and ⟨3D⟩ model structures, implying greater (in an absolute sense, i.e., more positive or more negative) ⟨3D⟩ NLTE abundance corrections, which was also demonstrated in Bergemann et al. (2017). For red giants, the ⟨3D⟩ NLTE corrections are ∼0.1 dex compared to 1D NLTE, while for metal-poor dwarfs they change in the opposite direction.

The differences between the trends have profound implications for chemical evolution models (of the Milky Way in this work, and, naturally, for other galaxies), because they imply different formation scenarios for the Galactic components. The declining 1D LTE [Mg/Fe] trend, seen already for [Fe/H] $\lesssim -2$ may suggest a very fast channel for SN Ia production, but this scenario is not supported by our 1D NLTE results, which instead point to a mass- and metallicity-dependent production of Mg in SNe II. In our most accurate ⟨3D⟩ NLTE results, which are are closest to full 3D NLTE, the halo and the thick disk clearly separate from one another in the [Mg/Fe]–[Fe/H] plane. Stars of the thick disk occupy a narrow band at a constant mean [Mg/Fe] of ∼0.3 dex. The thick disk extends to [Fe/H] ≈ -1.6, showing no trend of [Mg/Fe] with metallicity and an intrinsic dispersion of less than 0.03 dex, which argues againt the fast SN Ia channel. In contrast, the halo population shows a trend with [Fe/H], with a significant number of very metal-poor stars with high [Mg/Fe], but reaching to solar [Mg/Fe] values around [Fe/H] ≈ -1.0. This behavior is observed in dwarf galaxies, being due to the their high mass loss rates and very low star formation efficiencies.

Our results are still based on a small sample of stars and the fact that we use mean 3D hydrodynamical models. In this paper we employ only those Mg I lines that are least sensitive to the model physics, in particular the 5711 Å line, for which the 3D–⟨3D⟩ abundance differences are expected to be within 0.05 dex. Unfortunately, the few very metal-poor stars in our sample, which have very low (solar-like) ⟨3D⟩ NLTE [Mg/Fe] ratios, are also those where only the 5528 Å line could be measured in the spectra. Bergemann et al. (2017) showed that for this spectral line the abundances derived using full 3D NLTE calculations can be higher by up to +0.2 dex. Thus we cannot currently conclude on whether there are truly solar-like α-poor stars at very low [Fe/H] < -2 in the halo. Also, our sample was pre-selected against metal-rich stars, and there are only a few members of the thin disk, which does not allow us to probe the thin–thick disk transition.

Our study has demonstrated how vital full spectroscopic analysis is for the understanding of trends of abundance ratios with metallicity in different stellar components. The systematic biases inferred from simplifying assumptions (1D, LTE) are strong enough to force wrong formation scenarios in chemical evolution models. This paper also shows the urgent need to analyze all important elements in full 3D NLTE models, and to compare their results with Galaxy formation and chemical evolution models to test the validity of their assumptions and predictions.

We thank T. Gehren, and F. Grupp for providing the observed high-resolution data and stellar atmosphere models used in this work. R.C. acknowledges partial support from a DECRA grant from the Australian Research Council (project DE120102940). Funding for the Stellar Astrophysics Centre is provided by The Danish National Research Foundation. G.R. acknowledges support from the project grant "The New Milky Way" from the Knut and Alice Wallenberg Foundation. M.B. acknowledges support by the Collaborative Research center SFB 881 (Heidelberg University) of the Deutsche Forschungsgemeinschaft (DFG, German Research Foundation). This work was supported by the research grants (VKR023406, VKR023371) from Villum Fonden and from Augustinus Fonden. This work has made use of data from the European Space Agency (ESA) mission *Gaia* (http://www.cosmos.esa.int/gaia), processed by the *Gaia* Data Processing and Analysis Consortium (DPAC, http://www.cosmos.esa.int/web/gaia/dpac/consortium). Funding for the DPAC has been provided by national institutions, in particular the institutions participating in the *Gaia* Multilateral Agreement. M.B. thanks Brad Gibson and Gareth Few for useful discussions about the chemical evolution of the Galaxy and for pointing out the low-energy supernova scenario. We used the IDL software packages from the Coyote graphics library, IDL Astronomy User's Library, and http://www-astro.physics.ox.ac.uk/~mxc/software/.

Appendix

Figures 7 and 8 illustrate 1D NLTE and ⟨3D⟩ NLTE abundance corrections for the 5711 (left panel) and 5528

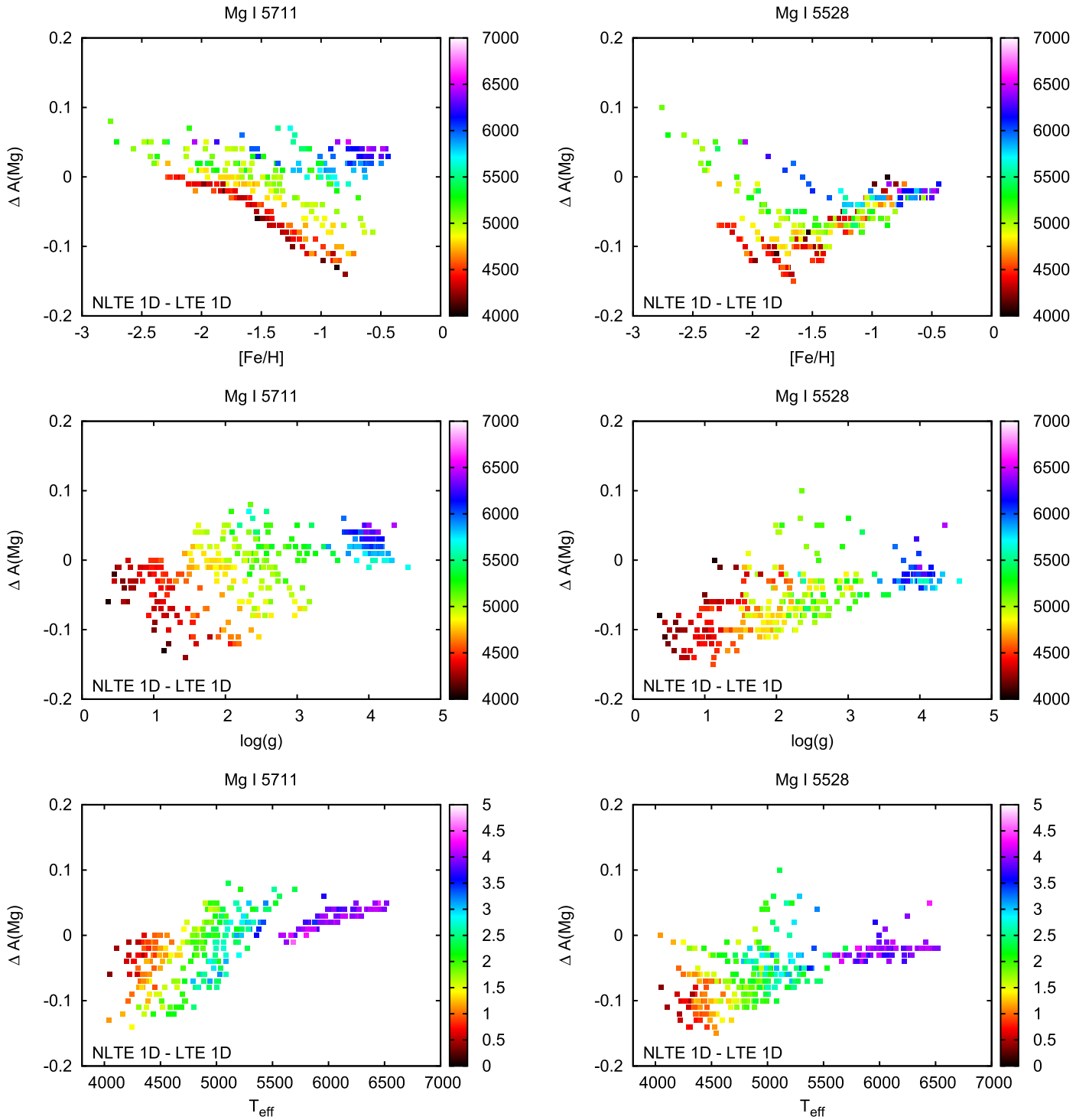

Figure 7. NLTE abundance corrections for the selected Mg I lines computed with 1D hydrostatic model atmospheres. The stars are color-coded with their values of $T_{\rm eff}$ (top and middle panels) and $\log g$ (bottom panels).

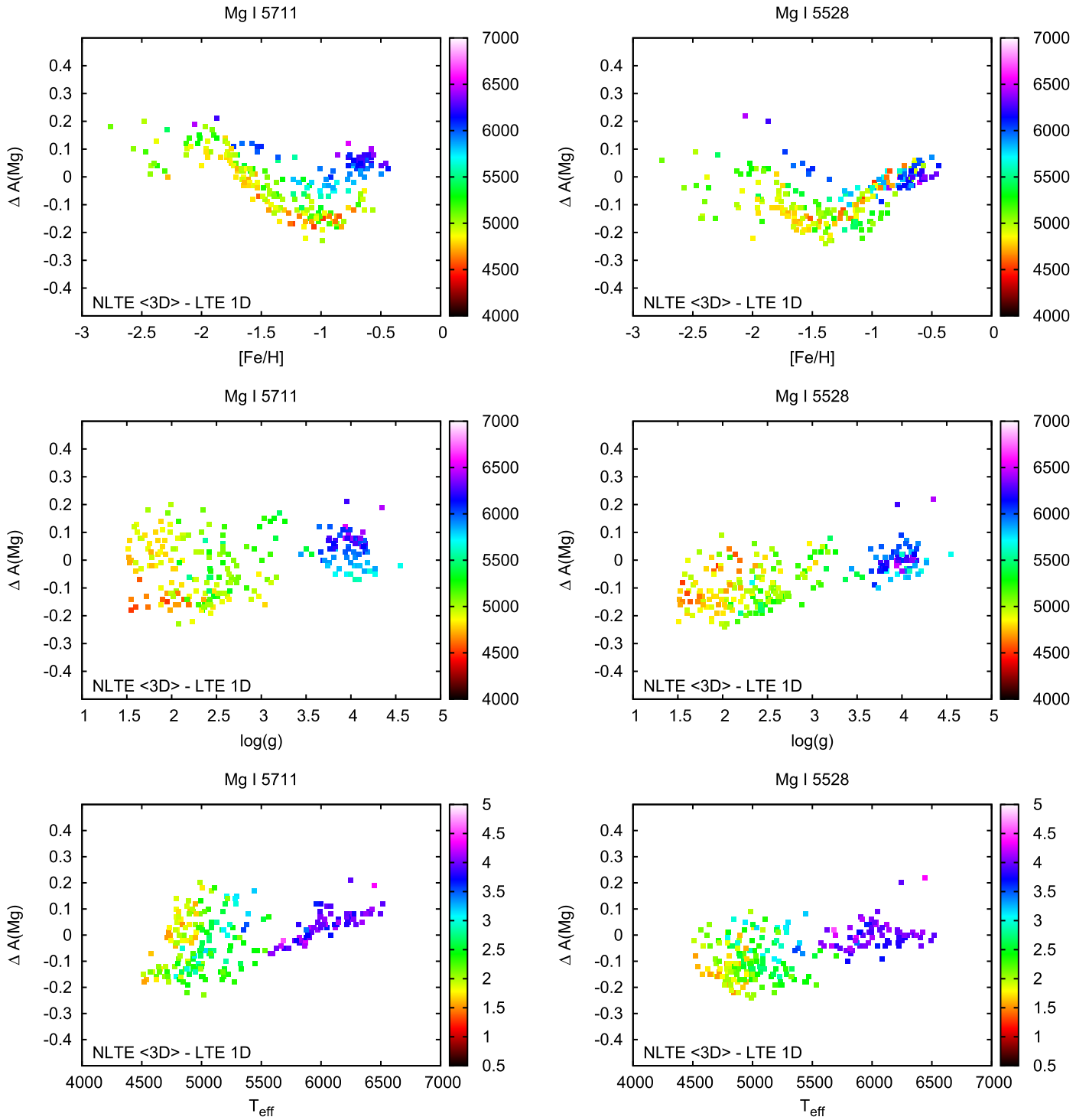

Figure 8. NLTE abundance corrections for the selected Mg I lines computed with ⟨3D⟩ model atmospheres. The stars are color-coded with their values of $T_{\rm eff}$ (top and middle panels) and $\log g$ (bottom panels).

(right panel) Å Mg I lines as a function of $T_{\rm eff}$, $\log g$, and [Fe/H].

ORCID iDs

Maria Bergemann https://orcid.org/0000-0002-9908-5571
Remo Collet https://orcid.org/0000-0001-6093-8402
Camilla Juul Hansen https://orcid.org/0000-0002-7277-7922

References

Argast, D., Samland, M., Gerhard, O. E., & Thielemann, F.-K. 2000, A&A, 356, 873
Argast, D., Samland, M., Thielemann, F.-K., & Gerhard, O. E. 2002, A&A, 388, 842
Barklem, P. S., Piskunov, N., & O'Mara, B. J. 2000, A&AS, 142, 467
Bensby, T., Feltzing, S., & Oey, M. S. 2014, A&A, 562, A71
Bergemann, M., Collet, R., Amarsi, A. M., et al. 2017, ApJ, 847, 15

Bergemann, M., Hansen, C. J., Bautista, M., & Ruchti, G. 2012a, A&A, 546, A90
Bergemann, M., Kudritzki, R.-P., Gazak, Z., Davies, B., & Plez, B. 2015, ApJ, 804, 113
Bergemann, M., Lind, K., Collet, R., Magic, Z., & Asplund, M. 2012b, MNRAS, 427, 27 (Paper 1)
Brusadin, G., Matteucci, F., & Romano, D. 2013, A&A, 554, A135
Butler, K., & Giddings, J. 1985, Newsletter on Analysis of Astronomical Spectra No. 9 (Univ. College London)
Cappellari, M., McDermid, R. M., Alatalo, K., et al. 2013, MNRAS, 432, 1862
Casagrande, L., Schönrich, R., Asplund, M., et al. 2011, A&A, 530, A138
Casagrande, L., & VandenBerg, D. A. 2014, MNRAS, 444, 392
Cescutti, G. 2008, A&A, 481, 691
Collet, R., Magic, Z., & Asplund, M. 2011, Journal of Physics Conf. Series, 328, 1
Conroy, C., Graves, G. J., & van Dokkum, P. G. 2014, ApJ, 780, 33
de Boer, T. J. L., Tolstoy, E., Lemasle, B., et al. 2014, A&A, 572, A10
Fuhrmann, K. 1998, A&A, 338, 161
Fuhrmann, K. 2004, AN, 325, 3
Gaia Collaboration, Brown, A. G. A., Vallenari, A., et al. 2016a, A&A, 595, A2
Gaia Collaboration, Prusti, T., de Bruijne, J. H. J., et al. 2016b, A&A, 595, A1
García Pérez, A. E., Allende Prieto, C., Holtzman, J. A., et al. 2016, AJ, 151, 144
Gilmore, G., & Wyse, R. F. G. 1998, AJ, 116, 748
Gonzalez, O. A., Rejkuba, M., Zoccali, M., et al. 2011, A&A, 530, A54
Gonzalez, O. A., Zoccali, M., Vasquez, S., et al. 2015, A&A, 584, A46
Grebel, E. K. 2005, in IAU Coll. 198, Near-fields Cosmology with Dwarf Elliptical Galaxies, ed. H. Jerjen & B. Cambridge (Cambridge: Cambridge Univ. Press), 1
Greene, J. E., Janish, R., Ma, C.-P., et al. 2015, ApJ, 807, 11
Greggio, L., & Renzini, A. 1983, A&A, 118, 217
Grupp, F. 2004a, A&A, 420, 289
Grupp, F. 2004b, A&A, 426, 309
Hansen, C. J., Bergemann, M., Cescutti, G., et al. 2013, A&A, 551, A57
Hansen, C. J., Primas, F., Hartman, H., et al. 2012, A&A, 545, A31
Holtzman, J. A., Shetrone, M., Johnson, J. A., et al. 2015, AJ, 150, 148
Karlsson, T. 2005, A&A, 439, 93
Karlsson, T., & Gustafsson, B. 2005, A&A, 436, 879
Kordopatis, G., Wyse, R. F. G., Gilmore, G., et al. 2015, arXiv:1507.08066
Lemasle, B., de Boer, T. J. L., Hill, V., et al. 2014, A&A, 572, A88
Limongi, M., & Chieffi, A. 2003, ApJ, 592, 404
Magic, Z., Collet, R., Asplund, M., et al. 2013, A&A, 557, A26
Mannucci, F., Della Valle, M., Panagia, N., et al. 2005, A&A, 433, 807
Mannucci, F., Della Valle, M., & Panagia, N. 2006, MNRAS, 370, 773
Mashonkina, L. 2013, A&A, 550, AA28
Matteucci, F. 2014, The Origin of the Galaxy and Local Group, Saas-Fee Advanced Course, Vol. 37 (Berlin: Springer), 145
Matteucci, F., Panagia, N., Pipino, A., et al. 2006, MNRAS, 372, 265
McWilliam, A., Matteucci, F., Ballero, S., et al. 2008, AJ, 136, 367
McWilliam, A., & Rich, R. M. 1994, ApJS, 91, 749
Munari, U., Henden, A., Frigo, A., et al. 2014, AJ, 148, 81
Ness, M., Zasowski, G., Johnson, J. A., et al. 2016, ApJ, 819, 2
Nissen, P. E., Gustafsson, B., Edvardsson, B., & Gilmore, G. 1994, A&A, 285, 440
Nissen, P. E., & Schuster, W. J. 2010, A&A, 511, L10
Onodera, M., Carollo, C. M., Renzini, A., et al. 2015, ApJ, 808, 161
Osorio, Y., Barklem, P. S., Lind, K., et al. 2015, A&A, 579, A53
Pehlivan Rhodin, A., Hartman, H., Nilsson, H., & Jönsson, P. 2017, A&A, 598, A102
Recio-Blanco, A., de Laverny, P., Kordopatis, G., et al. 2014, A&A, 567 A5
Ruchti, G. R., Bergemann, M., Serenelli, A., Casagrande, L., & Lind, K. 2013, MNRAS, 429, 126
Ruchti, G. R., Fulbright, J. P., Wyse, R. F. G., et al. 2011, ApJ, 737, 9
Schlafly, E. F., & Finkbeiner, D. P. 2011, ApJ, 737, 10
Schönrich, R., & Bergemann, M. 2014, MNRAS, 443, 698
Schönrich, R., & Binney, J. 2009a, MNRAS, 396, 203
Schönrich, R., & Binney, J. 2009b, MNRAS, 399, 1145
Serenelli, A. M., Bergemann, M., Ruchti, G., & Casagrande, L. 2013, MNRAS, 429, 3645
Shen, S., Cooke, R. J., Ramirez-Ruiz, E., et al. 2015, ApJ, 807, 115
Shetrone, M., Venn, K. A., Tolstoy, E., et al. 2003, AJ, 125, 684
Steinmetz, M., Zwitter, T., Siebert, A., et al. 2006, AJ, 132, 1645
Timmes, F. X., Woosley, S. E., & Weaver, T. A. 1995, ApJS, 98, 617
Tinsley, B. M. 1979, ApJ, 229, 1046
Tolstoy, E., Hill, V., & Tosi, M. 2009, ARA&A, 47, 371
Valenti, J. A., & Piskunov, N. 2012, SME: Spectroscopy Made Easy, Astrophysics Source Code Library ascl:1202.013
Venn, K. A., Irwin, M., Shetrone, M. D., et al. 2004, AJ, 128, 1177
Woosley, S. E., & Weaver, T. A. 1995, ApJS, 101, 181
Zwitter, T., Siebert, A., Munari, U., et al. 2008, AJ, 136, 421